

# Nanoscale

Accepted Manuscript



This is an *Accepted Manuscript*, which has been through the Royal Society of Chemistry peer review process and has been accepted for publication.

*Accepted Manuscripts* are published online shortly after acceptance, before technical editing, formatting and proof reading. Using this free service, authors can make their results available to the community, in citable form, before we publish the edited article. We will replace this *Accepted Manuscript* with the edited and formatted *Advance Article* as soon as it is available.

You can find more information about *Accepted Manuscripts* in the [Information for Authors](#).

Please note that technical editing may introduce minor changes to the text and/or graphics, which may alter content. The journal's standard [Terms & Conditions](#) and the [Ethical guidelines](#) still apply. In no event shall the Royal Society of Chemistry be held responsible for any errors or omissions in this *Accepted Manuscript* or any consequences arising from the use of any information it contains.

# Cell interaction with graphene microsheets: Near-orthogonal cutting versus parallel attachment

Xin Yi and Huajian Gao\*

Recent experiments indicate that graphene microsheets can either undergo a near-orthogonal cutting or a parallel attachment mode of interaction with cell membranes. Here we perform theoretical analysis to characterize the deformed membrane microstructure and investigate how these two interaction modes are influenced by the splay, tilt, compression, tension, bending and adhesion energies of the membrane. Our analysis indicates that, driven by the membrane splay and tension energies, a two-dimensional microsHEET such as graphene would adopt a near-perpendicular configuration with respect to the membrane in the transmembrane penetration mode; whereas the membrane bending and tension energies would lead to parallel attachment in the absence of cross membrane penetration. These interaction modes may have broad implications in applications involving drug delivery, cell encapsulation and protection, and measurement of dynamic cell response.

## 1 Introduction

Cell interaction with two-dimensional (2D) nanomaterials has attracted increasing attention in the areas of drug delivery, therapeutics, bioimaging, and nanotoxicity.<sup>1–3</sup> Typical 2D nanomaterials are plate-like materials with thickness at the nanoscale but lateral dimensions at a much larger scale, such as talc, mica nanosheets, boron nitride nanosheets, and graphene-family nanomaterials (GFNs) including graphene, graphene oxide (GO), reduced graphene oxide (rGO) and other related materials. Recent experiments, most related to GFNs, have indicated that size and surface properties of 2D nanomaterials play a critical role in their biological behavior.<sup>4–12</sup> For example, a combination of experiments and molecular dynamics simulations have demonstrated that pristine graphene and GO nanosheets can pierce into and destructively extract lipid molecules from the cell membranes of *Escherichia coli* bacteria, drastically reducing their viability.<sup>4</sup> The uptake of ultra-small polyethylene glycol (PEG) functionalized GO by liver and spleen is significantly higher than that of large rGO functionalized with PEG.<sup>5</sup> Much more cell viability loss is induced by small GO than large ones.<sup>6</sup> After attachment to cell membranes, small (500 nm lateral dimension) and large (1  $\mu\text{m}$ ) protein-coated GO nanosheets are internalized through clathrin-mediated endocytosis and phagocytosis, respectively.<sup>7</sup> Murine macrophages treated with graphene undergo a dose-dependent apoptosis;<sup>8</sup> while those incubated with GO elicit autophagy and toll-like receptor signaling cascades in their innate immune response.<sup>9</sup> Graphene shows little hemolysis of red blood cells which implies a low risk of thrombosis; while GO nanosheets are thrombogenic and those with smaller size exhibit higher hemolytic activity.<sup>10</sup> In addition, coating GO with chitosan, a biocompatible polymer, can eliminate hemolysis caused by GO nanosheets.<sup>10</sup>

In addition to extensive experiments on the biological behavior of 2D nanomaterials, a few studies, most employing

molecular simulations and targeting on small graphene and GO platelets,<sup>4,12–15</sup> have been focused on the modes of interaction between 2D nanomaterials and cell membranes. For example, it has been demonstrated by coarse-grained molecular dynamics (MD) simulations that a graphene nanoflake or microsHEET can spontaneously pierce into the lipid bilayer membrane at corners or asperities.<sup>12,13</sup> A similar behavior of graphene insertion into the lipid bilayer has also been observed in all-atom MD simulations.<sup>4</sup> Depending on the lateral size, graphene sheets can either cut across the membrane as a transmembrane object or align parallel at the interface between the two lipid monolayers.<sup>12–14</sup> Further investigations showed that graphene nanoflakes with 10% carbon atoms oxidized at edges form a transmembrane nanostructure; while those with 5% oxidized edge atoms stay parallel between two monolayers.<sup>13</sup> These different behaviors have been attributed to the interplay among the hydrophobic attraction between pristine graphene and lipid hydrocarbon chains, the hydrophilic attraction among oxidized regions, lipid heads and water, and the repulsion between hydrophobic and hydrophilic parts of the system.

Recently, a number of experimental studies have been conducted on the interaction between cell membranes and micro-sized GFNs.<sup>1,7,12</sup> It has been observed that graphene and few-layer graphene microsheets (0.5  $\mu\text{m}$  to 5  $\mu\text{m}$  lateral dimension) orient their surfaces nearly perpendicular to the membrane of human lung epithelial cells, primary human keratinocytes (Fig. 1a) and murine macrophages, after spontaneous membrane piercing at edge asperities or corner sites;<sup>12</sup> while human THP-1 macrophages exposed to 25  $\mu\text{m}$  few-layer graphene adhere and spread on the graphene surface (Fig. 1b).<sup>1</sup> Similar attachment of 2D nanomaterials onto cell membranes has been observed in cell uptake of protein-coated graphene oxide nanosheets.<sup>7</sup> These experiments suggest that there exist two basic modes of interaction between micro-sized 2D nanomaterials and cell membranes: near-perpendicular membrane penetration (schematically shown in Fig. 1c) after spontaneous piercing or parallel attachment

School of Engineering, Brown University, Providence, Rhode Island 02912, United States. E-mail: huajian\_gao@brown.edu

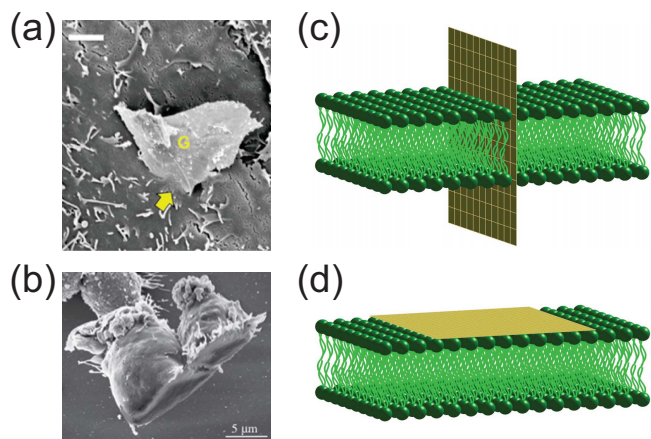


**Fig. 1** Modes of interaction between cell membranes and graphene microsheets. (a) Near-perpendicular penetration at a corner (yellow arrow) of graphene microsheets (G) into the membrane of a primary human keratinocyte (Scale bar,  $2 \mu\text{m}$ ). Adapted with permission from Ref. 12. Copyright 2013 National Academy of Sciences, USA. (b) Parallel attachment and spreading of macrophages on graphene microsheets. Adapted with permission from Ref. 1. Copyright 2012 American Chemical Society. (c,d) Schematic representations of the interaction modes exhibited in (a,b).

(Fig. 1d) onto the cell membranes. However, these different configurations of 2D nanomaterials and modes of interaction have not been thoroughly investigated. Here we present a theoretical model on the interaction between the cell membrane and a rigid micro-sized 2D nanomaterial with thickness comparable to that of the membrane and lateral dimension at a much larger length scale. In the following, we will characterize the microstructure of the deformed membrane, quantify its bending and membrane tension energy, and investigate how the interaction modes are influenced by these energy contributions. Some related biological implications are also discussed. For simplicity but without loss of generality, we will restrict our analysis in two dimensions and on symmetric lipid bilayer membranes composed of two lipid monolayers of the same composition.

## 2 Near-perpendicular membrane penetration mode

### 2.1 Model and methods

We first focus on the membrane penetration by 2D nanomaterials, such as a pristine graphene microsheet, whose surfaces are hydrophobic or can exhibit other specific adhesive interaction with the lipid tails. In this case, the length scale of the concerned local membrane deformation is comparable with the bilayer thickness and a model considering the molecular details of each monolayer is required. The elastic energy of a monolayer mainly results from the deformation of hydrocarbon chains.<sup>16,17</sup> To describe that local deformation and quantify the deformation energy, here we adopt

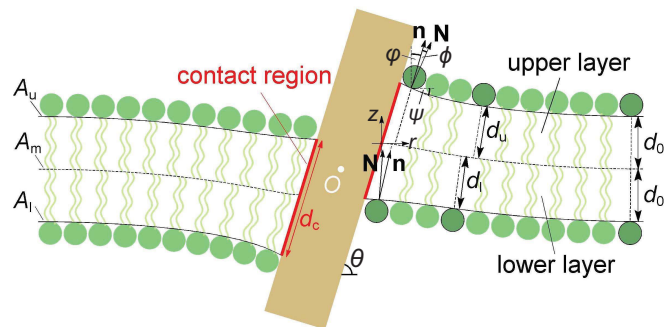


**Fig. 2** Schematics of an initially flat lipid bilayer (green) traversed by a rigid micro-sized 2D nanomaterial (brown) at an orientational angle  $\theta$ . Here,  $A_m$  denotes the midplane along the interface between two monolayers, and  $A_u$  and  $A_l$  the upper and lower surfaces dividing lipid heads and tails. The origin of the two-dimensional Cartesian coordinate  $rz$  is located at the point of intersection of the right-hand midplane and contact region;  $\psi$  is the tangent angle of the dividing surface whose unit normal vector is denoted by  $\mathbf{N}$ . In our notation, the angle  $\phi$  between the unit tail director  $\mathbf{n}$  and  $z$ -axis is positive as it is measured clockwise from the positive  $z$ -axis; angle  $\phi$  between  $\mathbf{n}$  and  $\mathbf{N}$  and tangent angle  $\psi$  are positive as measured counterclockwise from  $\mathbf{n}$  and the positive  $r$ -axis, respectively, for both upper and lower monolayers; accordingly, in Fig. 2 the angle on top marked by  $\phi$  has a positive value, and angles marked by  $\phi$  and  $\psi$  have negative values;  $d_c$  is the length of the contact region (red),  $d_0$  denotes the length of unperturbed tail chains, and  $d_u$  and  $d_l$  are the lengths of perturbed tail chains in the upper and lower monolayers, respectively.

an elastic continuum framework first proposed for studying lipid mesophase construction<sup>18,19</sup> and further developed in modeling lipid membrane fusion<sup>20,21</sup> and membrane-protein interaction,<sup>22</sup> where the effects of membrane bending, compression, and lipid orientation are considered. The structure of the lipid bilayer perturbed by the penetrated 2D nanomaterial is characterized by the shape of the midplane  $A_m$  defined as the interface between the lipid tail groups of the upper and lower monolayers, and the length  $d$  and orientation  $\mathbf{n}$  of the tail region of each lipid molecule (see Fig. 2). Hereafter, we use subscripts  $m$ ,  $u$ , and  $l$  to identify quantities associated with the midplane, upper monolayer, and lower monolayer, respectively. The midplane  $A_m$  is characterized by its position vector  $\mathbf{x}_m = \mathbf{x}_m(r_m, z_m)$  with Cartesian coordinate  $(r_m, z_m)$ . For the upper monolayer, the dividing surface  $A_u$  between the hydrophilic lipid heads and hydrophobic lipid tails (hydrocarbon chains) can be represented by a position vector  $\mathbf{x}_u = \mathbf{x}_u(r_u, z_u)$  whose coordinate  $(r_u, z_u)$  is determined as  $r_u = r_m + d_u \sin \phi_u$  and  $z_u = z_m + d_u \cos \phi_u$ . Here  $d_u$  is the length of the lipid tail and  $\phi_u$  is the angle between the unit tail director  $\mathbf{n}_u$  and the  $z$ -axis with a geometrical relation  $\mathbf{n}_u = \sin \phi_u \mathbf{e}_r + \cos \phi_u \mathbf{e}_z$  (Fig. 2),  $\mathbf{e}_r$  and  $\mathbf{e}_z$  being the unit base vectors along the coordinates  $r$  and  $z$ , respectively. The unit normal vector  $\mathbf{N}_u$  to the dividing surface  $A_u$  is determined by the tangent angle  $\psi_u$  of  $A_u$  as  $\mathbf{N}_u = -\sin \psi_u \mathbf{e}_r + \cos \psi_u \mathbf{e}_z$ , where  $\sin \psi_u = (dz_u/dr_u)/\sqrt{1+(dz_u/dr_u)^2}$  and  $\cos \psi_u =$

$1/\sqrt{1+(dz_u/dr_u)^2}$ . In general,  $\mathbf{n}_u \neq \mathbf{N}_u$  in the perturbed membrane and the angle  $\phi_u$  between them is  $\phi_u = \phi_u + \psi_u$ . Both  $\mathbf{n}_u$  and  $\mathbf{N}_u$  point toward the exterior of the bilayer membrane. For the lower monolayer,  $r_l = r_m - d_l \sin \phi_l$ ,  $z_l = z_m - d_l \cos \phi_l$ , and the unit tail director  $\mathbf{n}_l$  and unit normal vector  $\mathbf{N}_l$  of the dividing surface  $A_l$  are defined to point toward the interior of the membrane (see Fig. 2). Terms  $\mathbf{n}_l$ ,  $\mathbf{N}_l$ ,  $\sin \psi_l$ ,  $\cos \psi_l$ , and  $\phi_l$  have the same forms as those for the upper monolayer with the subscript ‘u’ replaced by ‘l’.

With the knowledge of the monolayer structure, the elastic free energy of a monolayer consisting of a certain amount of lipid molecules can be expressed as an integral  $\int_A f dA$ , where

$$f = \frac{1}{2}k(\text{div } \mathbf{n} - c_0)^2 - \frac{1}{2}kc_0^2 + \frac{1}{2}k_t \mathbf{t}^2 + \frac{K}{2} \left( \frac{d}{d_0} - 1 \right)^2 \quad (1)$$

is the elastic free energy per unit length of the monolayer. The first term in eqn (1) accounts for the splay energy of the lipid tail molecules, where  $k$  and  $c_0$  are the bending modulus and spontaneous curvature of the monolayer, respectively, and  $\text{div } \mathbf{n} = \cos \psi \cos \phi d\phi/dr$  is the divergence of the unit tail director  $\mathbf{n}$  along the dividing surface. In the case of vanishing tilt ( $\mathbf{t} = 0$  or  $\phi = 0$ ),  $\text{div } \mathbf{n} = -\cos \psi d\psi/dr$  reduces to the expression introduced in the classical Helfrich model.<sup>16</sup> The second term in eqn (1) is the ground state energy with vanishing splay and tilt ( $\text{div } \mathbf{n} = 0$  and  $\mathbf{t} = 0$ ) for the monolayer in a flat unperturbed membrane. The third term in eqn (1) represents the tilt energy of lipid molecules where  $k_t$  is the tilt modulus of the monolayer and  $\mathbf{t}$  is the tilt vector defined as

$$\mathbf{t} = \frac{\mathbf{n}}{\mathbf{n} \cdot \mathbf{N}} - \mathbf{N} = \tan \phi \mathbf{e}_\psi,$$

which is parallel to,  $\mathbf{e}_\psi = \cos \psi \mathbf{e}_r + \sin \psi \mathbf{e}_z$ , the unit tangent vector of the dividing surface, characterizing the deviation of the tail director  $\mathbf{n}$  from the surface normal  $\mathbf{N}$ . Note that the quadratic form of the tilt energy requires the magnitude of  $\mathbf{t}$  staying small, that is,  $|\mathbf{t}| < 1$ . The last term in eqn (1) denotes compression energy of the lipid molecules where  $d$  and  $d_0$  are the lengths of perturbed and unperturbed tail chains, respectively, and  $K$  is the out-of-plane compressibility modulus of the monolayer, which is equivalent to its lateral area compressibility modulus. In general, the bending and compressibility moduli  $k$  and  $K$  of a monolayer can be taken as approximately half those of the bilayer.<sup>20,21</sup> In the case of strong adhesive interaction, the lipid tails of either one or both monolayers near the contact regions would be stretched as long as possible before they are broken or extracted out of the bilayer. Here, the maximum length of a stretched lipid hydrocarbon chain is chosen as  $\max\{d\} = 1.3d_0$  based on the thickness variation of a bilayer membrane induced by transmembrane proteins.<sup>23,24</sup> In our notation, the angle  $\phi$  between  $\mathbf{n}$  and  $z$ -axis is positive as it is measured clockwise from the positive  $z$ -axis. Based on this notation, the spontaneous curvature  $c_0$  in eqn (1) for the upper monolayer is consistent with the conventional definition of a spontaneous monolayer curvature; while for the lower monolayer  $c_0$  takes the opposite value of the spontaneous curvature.

For example, the spontaneous curvature of a DOPC monolayer is about  $-0.11 \text{ nm}^{-1}$ ,<sup>25</sup> so that  $c_0 = -0.11 \text{ nm}^{-1}$  for the upper DOPC monolayer and  $c_0 = 0.11 \text{ nm}^{-1}$  for the lower DOPC monolayer. It is also noted that the spontaneous curvature of the symmetric bilayer under consideration is zero regardless of the value of  $c_0$ . Since the membrane deforms in 2D, there is no energy term associated with the Gaussian curvature. In general, the volume of each lipid chain is considered as being conserved as the membrane deforms,<sup>26</sup> i.e. the lipid chains shrink laterally under stretch but swell under compression. Theoretical analysis indicated that the volume conservation only results in a higher than quadratic energy term,<sup>21,27</sup> which is neglected here. Since the lateral area compressibility modulus  $K$  is much larger than the tilt modulus  $k_t$  ( $K \gg k_t$ ) and bending modulus ( $K \gg k/d_0^2$ ),<sup>19,28</sup> the lateral deformation of membrane is negligible. Therefore, we assume that the cross-section area of each lipid molecule remain constant along the dividing surface, i.e. the monolayer does not undergo lateral stretching,<sup>18,20</sup> and that there is no void within the region of hydrocarbon chains.

Since the lipid molecules on both sides of the 2D nanomaterial can slide freely along it at some orientational angle  $\theta$ , the membrane would form an antisymmetric configuration with respect to the point  $O$  at the minimum energy state (Fig. 2). Our analysis therefore is focused on the right part of the bilayer. Since the system energy at angles  $\theta$  and  $\pi - \theta$  should be the same, it suffices to consider  $\theta \in [0, \pi/2]$ . The total free energy  $E_{\text{tot}}$  accounting for the deformation of the perturbed bilayer membrane and its interaction with the penetrating 2D nanomaterial is<sup>18–22,29</sup>

$$E_{\text{tot}} = 2 \times \left( \int_{A_u} f_u dA_u + \int_{A_l} f_l dA_l + \sigma \Delta A_m - \gamma d_c \right). \quad (2)$$

The prefactor 2 in eqn (2) stems from equal energy contributions from the right and left bilayers. The first two terms in the parentheses correspond to the elastic free energy of the upper and lower monolayers, each consisting of a given amount of lipid molecules. Physiologically, cells regulate and maintain an approximately constant value of the intrinsic membrane tension by adjusting the membrane area through exchange with lipid reservoirs. This effect is characterized by the third term in eqn (2), corresponding to the membrane tension energy in terms of the membrane tension  $\sigma$  and conjugated excess length  $\Delta A_m$  of the midplane  $A_m$ ,  $\Delta A_m = \int_{A_m} [\sqrt{1+(dz_m/dr_m)^2} - 1] dr_m$ . The last term in eqn (2) represents the adhesive interaction between the 2D nanomaterials and adjacent lipid tail groups;  $\gamma$  is the effective adhesion energy in which the membrane line tension at the contact region is implicitly included and  $d_c$  is the length of the contact region. Since the thickness of lipid head groups can be assumed constant, the interaction energy between the 2D nanomaterial and adjacent lipid heads only results in an additive constant energy term and is therefore neglected in eqn (2). It is worth noting that although the repulsive interaction energy between lipid heads and 2D nanomaterial has no influence on the minimum energy state, it forms an energy barrier and thus plays

an important role at the initial piercing of the 2D nanomaterial into the membrane.<sup>4,12,13</sup>

Here, we employ a numerical optimization technique to determine the minimum state of the total free energy at a given orientational angle  $\theta$ . Recalling the geometric relations mentioned in the preceding paragraph before eqn (1), the total free energy in eqn (2) can be expressed as a function of the unknown variables,  $z_m(r_m)$ ,  $d_u(r_m)$ ,  $\varphi_u(r_m)$ ,  $d_l(r_m)$ ,  $\varphi_l(r_m)$ , which are approximated by cubic B-spline curves. For example,  $z_m(r_m)$  can be parameterized as  $z_m(r_m) = \sum_{i=0}^L a_i N_i(r_m)$ , where the control points  $a_i$  are coefficients of the basis functions  $N_i(r_m)$  with  $L$  chosen as  $L = 56$  in our calculations. The basis functions  $N_i(r_m)$  are determined explicitly by specifying a knot vector  $\{r_m^{(0)}, \dots, r_m^{(L+4)}\}$ .<sup>30</sup> A typical choice is taken here as  $r_m^{(i)} = 0$  ( $i = 0, \dots, 3$ ) and  $r_m^{(i)} = r_{\text{end}}$  ( $i = L + 1, \dots, L + 4$ ), where  $r_{\text{end}}$  is the length of the midplane projection on each side and is set to be  $40d_0$  to approximate the remote boundary  $r_m \rightarrow \infty$ .

The boundary conditions provide either input parameters or equality constraints during energy minimization. At  $r_m = 0$ ,  $\varphi_u(0) = \varphi_l(0) = \pi/2 - \theta$  and  $d_u(0) + d_l(0) = d_c$  ensure that no voids exist between the 2D nanomaterial and adjacent lipid tails. At the remote boundary  $r_m \rightarrow \infty$ , the bilayer patch joins an flat and unperturbed membrane, with conditions  $\varphi_u = \varphi_l = 0$  and  $d_u = d_l = d_0$ . It is noted that at  $r_m \rightarrow \infty$  the condition  $\varphi_u = \varphi_l = 0$  does not imply  $\psi_u = \psi_l = 0$ ; and  $z_m$  at the remote boundary should have the same value for the left and right bilayers. To prevent penetration of adjacent lipid molecules, two inequality constraints are imposed:  $\cos \varphi_u + d_u(d\varphi_u/dr_m) - \sin \varphi_u(dz_m/dr_m) > 0$  for the upper monolayer and  $\cos \varphi_l - d_l(d\varphi_l/dr_m) - \sin \varphi_l(dz_m/dr_m) > 0$  for the lower one. The total free energy  $E_{\text{tot}}$  as a function of  $z_m, d_u, \varphi_u, d_l, \varphi_l$  under these constraints at a given  $d_c$  is minimized with respect to the control points using sequential quadratic programming<sup>31</sup> with an error tolerance of  $1 \times 10^{-6}$ . Meanwhile the structure of the bilayer characterized by  $z_m, d_u, \varphi_u, d_l, \varphi_l$  is determined at the state of minimum total free energy.

## 2.2 Results and discussion

Taking typical parameter values as  $k = 10 k_B T$ ,  $c_0 = 0$ ,  $k_t = 10 k_B T/\text{nm}^2$ ,<sup>19</sup>  $K = 30 k_B T/\text{nm}^2$ ,<sup>28</sup>  $d_0 = 1.4 \text{ nm}$ , and  $\max\{d\} = 1.3d_0$ , contours of the total free energy  $E_{\text{tot}}$  in eqn (1) at  $\sigma = 1 k_B T/\text{nm}^2$  is plotted as a function of the orientational angle  $\theta$  and adhesion energy  $\gamma$  in Fig. 3. The size of the contact region increases as adhesion energy  $\gamma$  increases, until around  $\gamma = 5.05 k_B T/\text{nm}^2$  when the stretched lipid tails in both upper and lower monolayers reaches the predefined limiting length  $\max\{d\} = 1.3d_0$  at any  $\theta$ . At larger  $\gamma$ , the size of the contact region would remain as  $d_c = 2.6d_0$ . Therefore, further increase in  $\gamma$  would only contribute to the linear adhesion energy term  $-2\gamma d_c$ . Figure 3 indicates that the configuration with  $\theta = 90^\circ$  always corresponds to a minimum energy state. A very small energy gradient in the range of

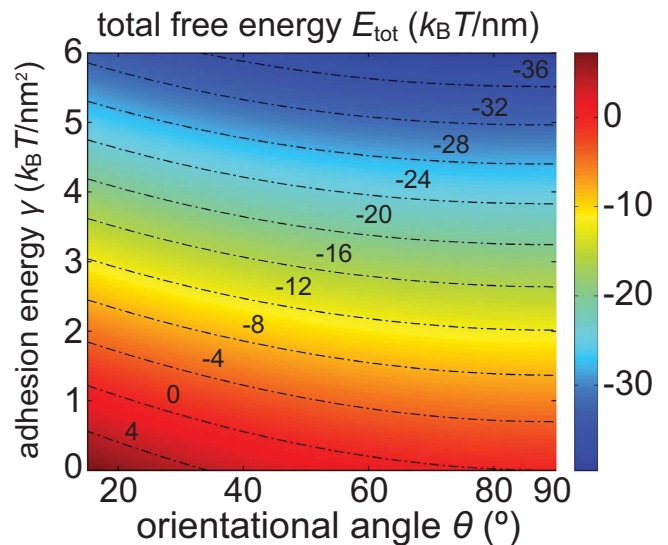


**Fig. 3** Contours of the total free energy  $E_{\text{tot}}$  as a function of the orientational angle  $\theta$  and adhesion energy  $\gamma$ .

$75^\circ \leq \theta \leq 90^\circ$  suggests that in the presence of thermal fluctuation the orientation of the micro-sized transmembrane 2D nanomaterial would be almost equally probable to occur for  $75^\circ \leq \theta \leq 90^\circ$  and thus a near-perpendicular configuration prevails around  $90^\circ$ . In this sense, the entry angle may not be strictly equal to  $90^\circ$  in experiments. This prediction is consistent with recent experimental and molecular simulation observations that few-layer graphene sheets adopt a nearly perpendicular surface orientation with respect to the membranes of human lung epithelial cells, murine macrophages and primary human keratinocytes.<sup>12</sup> The choice of the specific value  $\max\{d\} = 1.3d_0$  has only slight influence on the value of  $E_{\text{tot}}$  and does not affect the conclusion that a micro-sized rigid transmembrane 2D nanomaterials would rotate to a configuration with an orientational angle around  $\theta = 90^\circ$ . Further calculations indicate that a spontaneous curvature only has slight effects on the total free energy. A similar energy contour is observed in the case of  $\sigma = 0$ .

Selective configurations of a membrane with  $\sigma = 1 k_B T/\text{nm}^2$  being penetrated by a 2D nanomaterial at  $\theta = 60^\circ$  and  $90^\circ$  are shown in Fig. 4a. At  $\theta = 90^\circ$ , the membrane adopts a symmetric configuration with respect to the horizontal midplane. As  $\theta$  decreases, the midplane becomes curved and the bilayers on the left and right sides slide along the nanomaterial surface in opposite directions. This phenomenon results from the remote boundary conditions that  $\varphi_u = \varphi_l = 0$  and  $z_m$  at  $|r_m| \rightarrow \infty$  have the same value for both left and right bilayers. At a given  $\theta$ , membranes with different  $\sigma$  have similar configurations but different relative sliding distances whose values are inversely proportional to  $\sigma$ . A similar relative membrane sliding is observed in a recent MD simulation where a folded graphene with a small flake glued at one end pierces and fully penetrates a lipid bilayer (see Fig. S7 in Ref. 12).

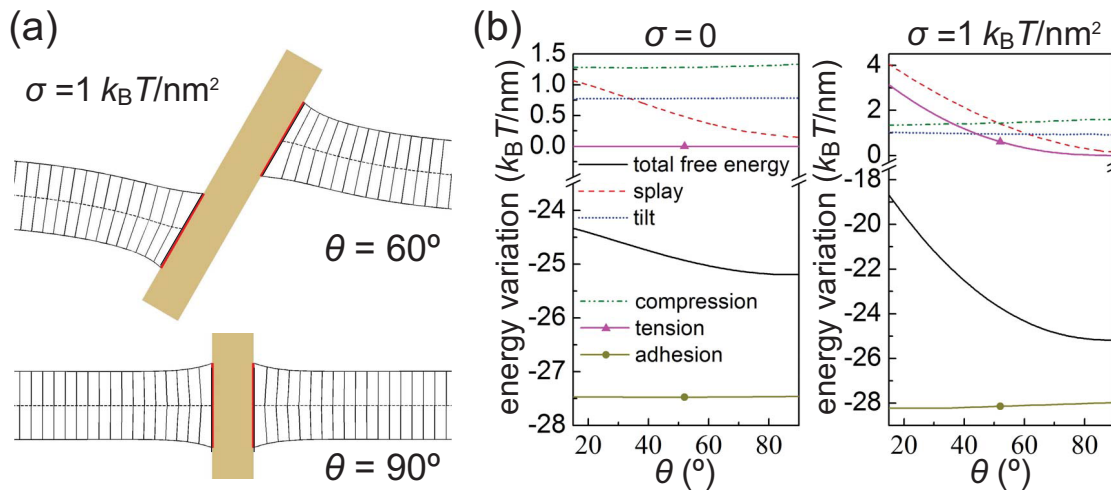


**Fig. 4** (a) Selective configurations of the transmembrane 2D nanomaterial and cell membrane with  $\sigma = 1 k_B T / \text{nm}^2$  at  $\theta = 60^\circ$  and  $90^\circ$ . (b) Variations of the total free energy and its five components as a function of  $\theta$  at  $\sigma = 0$  and  $\sigma = 1 k_B T / \text{nm}^2$ . In both (a) and (b),  $\gamma = 4 k_B T / \text{nm}^2$ .

The total free energy given in eqn (1) and (2) can be decomposed into five components, namely the splay, tilt, compression, membrane tension, and adhesion energies. To find out how these energy components regulate the nanomaterial orientation and affect the bilayer structure, we plot their variations along with that of the total free energy as functions of  $\theta$  (see Fig. 4b). It can be seen that the tilt, compression, and adhesion energies almost remain constant as  $\theta$  varies, regardless of the value of membrane tension. The total energy decreases as the micro-sized rigid transmembrane 2D nanomaterial rotates toward  $\theta = 90^\circ$  and reaches a minimum value at  $\theta = 90^\circ$ . The driving force toward the orthogonal configuration of  $\theta = 90^\circ$  comes from both splay and membrane tension energies. In the limit of  $\sigma = 0$ , the tension energy vanishes and splay energy alone acts as the main driving force for the  $\theta = 90^\circ$  configuration. Similar to the energy profile in Fig. 3, the very small energy gradient in the range of  $75^\circ \leq \theta \leq 90^\circ$  suggests that the 2D nanomaterial would undergo substantial thermal oscillations in that range and that a near-perpendicular orientation is preferred with the 2D nanomaterial tilting  $15^\circ$  or less from  $\theta = 90^\circ$ . Relatively high compression and adhesion energies indicate a large contact region and large variation in lipid lengths; a relatively high splay energy means a rapid variation of lipid orientation along the upper and lower dividing surfaces; a relatively high tilt energy means a large difference between the lipid orientation and normal of the dividing surface; a relatively high tension energy associated with a large membrane tension results in a relatively flat midplane. Therefore, a rough structure of the perturbed bilayer can be derived from the relative magnitudes of these five energy components. A comparison of the magnitudes of these five energy components indicates that, beside the splay, compression, and tension energies,<sup>29,32,33</sup> tilt energy plays an important role in the structural formation of the perturbed bilayer (see Fig. 4b). As  $\theta$  approaches  $90^\circ$ , the splay and tension energies becomes

less important, and the lipid structure of membrane becomes dominated by the lipid length variation and lipid tilt. Therefore, although it has negligible influence on the rotation of a transmembrane nanomaterial, the tilt energy has significant influence on the bilayer structure, especially as  $\theta$  approaches  $90^\circ$  (see Fig. 4b). The minor effect of splay and tension energies on the bilayer structure at  $\theta = 90^\circ$  is illustrated in Fig. 4a where lipid chains near the contact region are almost perpendicular to the horizontal midplane.

The perpendicular configuration ( $\theta = 90^\circ$ ) of a micro-sized transmembrane 2D nanomaterial corresponds to the minimum energy state. It would be useful to have an analytical scaling behavior for such an important case. Due to the configurational symmetry with respect to the  $r$ - and  $z$ -axes, we focus on the right upper monolayer and  $E_{\text{el}} \equiv E_{\text{tot}} + 2\gamma d_c = 4 \int_{A_u} f_u dA_u$  is four times the elastic energy of the right upper monolayer. At  $\theta = 90^\circ$ , the tension energy vanishes as the midplane is horizontal. Inspired by the slight orientation of lipid chains and minor contributions from the splay energy at  $\theta = 90^\circ$ , we first develop a very simple estimation in which we assume that all lipid chains are perpendicular to the horizontal midplane ( $\phi = 0$ ) and that the variation rate of monolayer thickness is so small that  $dz_u/dr_m \ll 1$  and  $\cos \phi \approx 1$ ;  $f_u$  given in eqn (1) is then reduced to  $f_u = \frac{k_t}{2} (dz_u/dr_m)^2 + \frac{K}{2} (z_u/d_0 - 1)^2$ . Variation of  $E_{\text{tot}}$  with respect to  $z_u$  leads to  $z_u = (d_c/2 - d_0) \exp[-\sqrt{K/(k_t d_0^2)} r_m] + d_0$ , where the boundary conditions  $z_u(r_m = 0) = d_c/2$  and  $z_u(r_m \rightarrow \infty) = d_0$  are used. With the knowledge of  $z_u$ ,  $E_{\text{el}}$  is given as

$$E_{\text{el}} = 2d_0 K \left( \frac{k_t}{K} \right)^{1/2} \left( \frac{d_c}{2d_0} - 1 \right)^2. \quad (3)$$

Our assumption on the perpendicular orientation of lipid chains can be regarded as an extra constraint which would result in a higher  $E_{\text{el}}$  as expressed in eqn (3).

One can also turn to another simplified model neglecting the tilt energy ( $k_t = 0$ ), which is widely employed in the studies of protein-membrane interactions.<sup>29,32,33</sup> We further take  $c_0 = 0$  for simplicity. Since the tilt energy is ignored in this case, the lipid chains can adopt their orientation freely and a configuration perpendicular to the midplane is favorable due to its minimum requirement of compression energy. With assumptions of  $dz_u/dr_m \ll 1$  and  $\cos\phi \approx 1$ ,  $f_u$  reduces to  $f_u = \frac{k}{2}(d^2z_u/dr_m^2)^2 + \frac{K}{2}(z_u/d_0 - 1)^2$ . Variation of  $E_{el}$  with respect to  $z_u$  and boundary conditions  $z_u(r_m = 0) = d_c/2$  and  $z_u(r_m \rightarrow \infty) = d_0$  collectively result in  $z_u = z_u(\eta)$  and then  $E_{el} = E_{el}(\eta)$ . The unknown parameter  $\eta$  is determined by  $dE_{el}(\eta)/d\eta = 0$ . After that,  $E_{el}$  can be represented as

$$E_{el} = \sqrt{2}d_0K \left( \frac{k}{Kd_0^2} \right)^{1/4} \left( \frac{d_c}{2d_0} - 1 \right)^2. \quad (4)$$

A similar method has been used to study the protein-induced bilayer deformations in axisymmetric configuration, where the deformation energy can also be expressed as a quadratic function of the lipid length variation.<sup>32,33</sup> Note that  $E_{el}$  in eqn (4) is expected to be underestimated due to the omission of tilt energy.

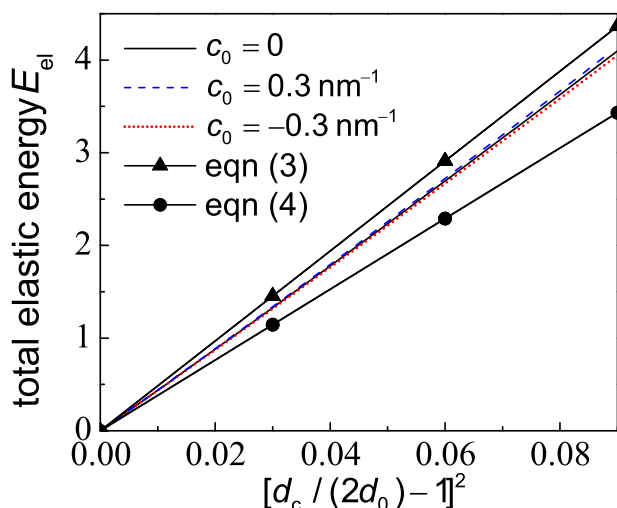


**Fig. 5** Total elastic energy  $E_{el}$  as a function of the lipid length variation at  $\theta = 90^\circ$ .

Combination of eqn (3) and (4) suggests a scaling of  $E_{el}$  as

$$E_{el} \sim Hd_0K[d_c/(2d_0) - 1]^2, \quad (5)$$

where the prefactor  $H = H(k_tK^{-1}, kK^{-1}d_0^{-2})$  is a function of the dimensionless parameters  $k_t/K$  and  $k/(Kd_0^2)$ . Figure 5, showing that  $E_{el}$  scales as  $\sim [d_c/(2d_0) - 1]^2$  and is bounded by eqn (3) and (4), confirms the validity of eqn (5) as well as the overestimation of  $E_{el}$  in eqn (3) and underestimation in eqn (4). The relatively large deviation between eqn (4) and the exact solution indicates again that the lipid tilt plays an important role in the membrane deformation at  $\theta = 90^\circ$ . As shown in Fig. 5, the spontaneous curvature has slight influence on the deformation energy. Here we only consider the

case  $d_c/(2d_0) \geq 1$ , and the results show that the elastic energy profile corresponding to a larger spontaneous curvature has a larger slope. For readers who are interested in the case of  $d_c/(2d_0) < 1$ ,  $E_{el}$  still scales as  $\sim [d_c/(2d_0) - 1]^2$  but with a slightly smaller slope compared with the case of  $d_c/(2d_0) \geq 1$ , and the energy profile of a larger  $c_0$  has a smaller slope.

A potential application of transmembrane 2D nanomaterials is drug delivery. By shrinking graphene liquid capsules,<sup>34</sup> DNA or specific molecules contained in these capsules can be transmitted through a transmembrane nanochannel into cells. The transmembrane 2D nanomaterials can also be employed in atomic force microscopy based nanoshaving lithography to selectively remove the target lipid patch.<sup>35</sup> Inclined transmembrane 2D nanomaterials would exhibit a rotation behavior toward to the near-perpendicular configuration, whose rate depends on the viscosity of the lipid bilayer. This provides a potential approach to measure the membrane viscosity through the dynamics of the rotation behavior.

### 3 Parallel attachment mode

#### 3.1 Model and methods

As another important mode of interaction, parallel attachment of micro-sized 2D nanomaterials on cell membranes has also been observed experimentally in cell uptake of protein-coated GO nanosheets.<sup>7</sup> For the transmembrane-penetration mode, the membrane thickness and scales of local membrane deformation are comparable, and the penetration is driven by the (hydrophobic) attraction between lipid tails (interior of the bilayer) and nanomaterial surface. By contrast, the parallel attachment mode is mostly facilitated by the hydrophilic or highly specific attraction between the bilayer surface and nanomaterial surface. Besides, the length scale of membrane deformation in the parallel attachment mode is much larger than the membrane thickness. Therefore, the cell membrane can be simply modeled as a smooth and structureless surface with consideration of bending and tension energies.<sup>16</sup> Without loss of generality, we consider the attachment of a semi-infinite 2D nanomaterial with a rounded end onto an initially flat membrane (Fig. 6).

The total energy of the system per unit length is described by the Canham-Helfrich functional as<sup>16,36–38</sup>

$$E_{tot} = \frac{\kappa}{2} \int \psi^2 ds + \sigma \Delta l - \gamma l_c, \quad (6)$$

where  $E_b = \frac{\kappa}{2} \int \psi^2 ds$  is the bending energy,  $\gamma$  is the adhesion energy, and  $l_c$  is the length of the contact region;  $\sigma$  is the membrane tension which is conjugated to the excess length  $\Delta l = \int (1 - \cos \psi) ds$  induced by wrapping;  $\psi$ ,  $s$ , and  $\kappa$  are the tangent angles, arclength, and bending stiffness of the membrane (see Fig. 6). The superimposed dot in the first term in eqn (6) denotes derivative with respect to the arclength  $s$ . For a bilayer membrane composed of two chemically identical monolayers as considered here, its bending stiffness  $\kappa$  is twice that of each monolayer ( $\kappa = 2k$  with  $k$  as the monolayer

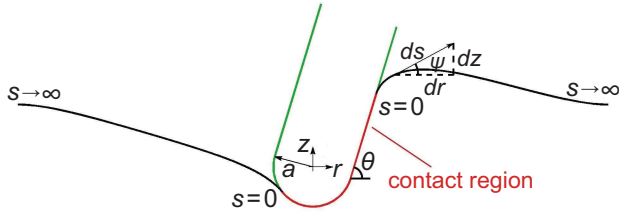


**Fig. 6** Schematics of adhesive attachment of a rigid 2D nanomaterial onto a lipid membrane. The 2D nanomaterial has a thickness  $2a$  with an orientational angle  $\theta$ . The rounded cap occupies the region with  $r^2 + z^2 \leq a^2$  and  $z \sin \theta + r \cos \theta \leq 0$  in the adopted coordinate  $rz$ ;  $\psi$  is the tangent angle and  $s$  denotes the arclength of the free membrane part from the contact edges  $s = 0$  to outer boundaries  $s \rightarrow \infty$ .

bending stiffness) and its spontaneous curvature is zero. All lengths are scaled by  $a$ , the half thickness of the nanomaterial (Fig. 6). Other dimensionless parameters are

$$\bar{\sigma} \equiv 2\sigma a^2/\kappa \quad \text{and} \quad \bar{\gamma} \equiv 2\gamma a^2/\kappa.$$

It is known that the equilibrium time scale of a lipid membrane subjected to various types of loading is less than one second, much shorter than that of cell uptake of nanomaterials varying from hundreds of seconds to tens of minutes.<sup>39</sup> Therefore, cellular uptake of nanomaterials can usually be regarded as a process limited by receptor diffusion toward the contact region.<sup>39–41</sup> Due to such a limited rate of receptor diffusion, we can focus on a short time scale and assume that the total length  $l_c$  of the contact region is fixed as the micro-sized 2D nanomaterial adjust its orientational angle  $\theta$  to reduce the total elastic energy  $E_{\text{el}} \equiv E_{\text{tot}} + \gamma l_c$ .

We employ sequential quadratic programming<sup>31</sup> to determine the minimum energy state at a given size of the contact region. The shape of the attached membrane is determined by that of the contact region. With geometric relations  $dr/ds = \cos \psi$  and  $dz/ds = \sin \psi$ , the shape of the outer free membrane on the left and right sides can be determined by  $\psi$  which is approximated by a Fourier series as<sup>38,42</sup>

$$\psi(s) = \psi_0 + (\psi_1 - \psi_0) \frac{s}{l} + \sum_{i=1}^N a_i \sin\left(\pi i \cdot \frac{s}{l}\right). \quad (7)$$

Here  $N$  is the number of Fourier modes chosen as  $N = 80$  in our calculations,  $a_i$  are the Fourier amplitudes,  $s$  is the arclength, and  $l$  is the membrane length on the side under consideration;  $\psi_0$  and  $\psi_1$  are the tangent angles at  $s = 0, l$ , respectively. To approximate the condition  $s \rightarrow \infty$ , the length  $l$  of each outer membrane region is treated as an unknown parameter determined by a large prescribed length of the membrane projection, which is set to be  $35a$ .

The boundary and constraint conditions provide either input parameters or equality constraints during energy minimization. At  $s \rightarrow \infty$ , the outer free membrane becomes asymptotically flat, which requires  $\psi_1 = 0$ . The continuity of the

coordinate  $(r, z)$  and tangent angles  $\psi$  at the left and right contact edges are enforced as equality constraints. The elastic energy as a function of  $\psi(s)$  under these constraints at a given  $l_c$  is minimized with respect to the Fourier amplitudes  $a_i$ , tangent angles  $\psi_0$  and  $\psi_1$  at both contact edges, and  $l$  for both outer free regions. Once the tangent angles  $\psi$  given by eqn (7) are known, the elastic energy and corresponding shapes of the membrane can be determined. Here we choose  $\psi = \psi(s)$  as the membrane parameterization to handle the case where one value of  $r$  might correspond to several values of  $z$ . That scenario, however, is not observed in our results shown below, which means that a form based on the Cartesian coordinate  $(r, z(r))$  is actually sufficient for the present analysis.

### 3.2 Results and discussion

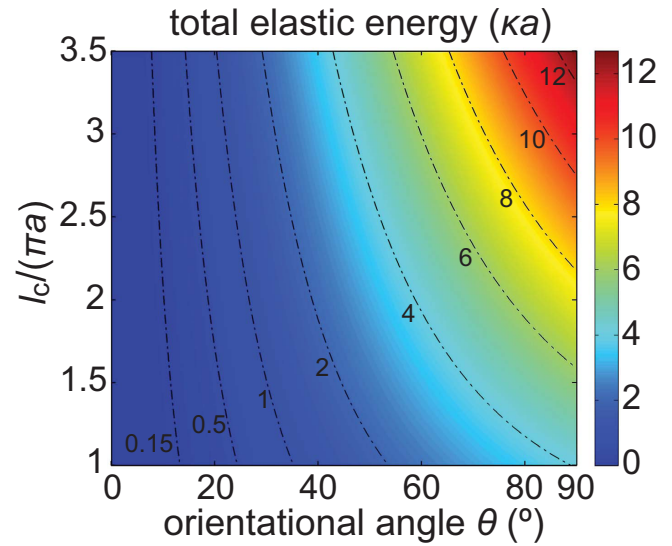


**Fig. 7** Contours of the normalized total elastic energy  $E_{\text{el}}/(\kappa a)$  as a function of the orientational angle  $\theta$  and normalized contact length  $l_c/(\pi a)$  at  $\bar{\sigma} = 2$ .

Figure 7 shows contours of the total elastic energy  $E_{\text{el}} \equiv E_{\text{tot}} + \gamma l_c$  in eqn (6) as a function of the orientational angle  $\theta$  and normalized contact length  $l_c/(\pi a)$ . A short time period of membrane wrapping immediately after the initial contact between the 2D nanomaterial and cell membrane is a highly dynamic process and does not principally apply to our assumption that  $l_c$  could be regarded as a constant. The contact length  $l_c$  in Fig. 7 is therefore restricted to relatively large values. It is shown that the configuration with  $\theta = 0^\circ$  always corresponds to a minimum energy state regardless of the value of the contact length. This result is also observed at very small  $l_c$  if the assumption of a fixed  $l_c$  is persisted in during the stage of the initial contact.

Configurations of a 2D nanomaterial wrapped by a membrane with  $\bar{\sigma} = 0.1$  and 2 at  $\theta = 30^\circ, 60^\circ$  and  $90^\circ$  are shown in Fig. 8a. The asymmetric configuration of the deformed membrane at  $\theta = 90^\circ$  is attributed to the fact that a symmet-

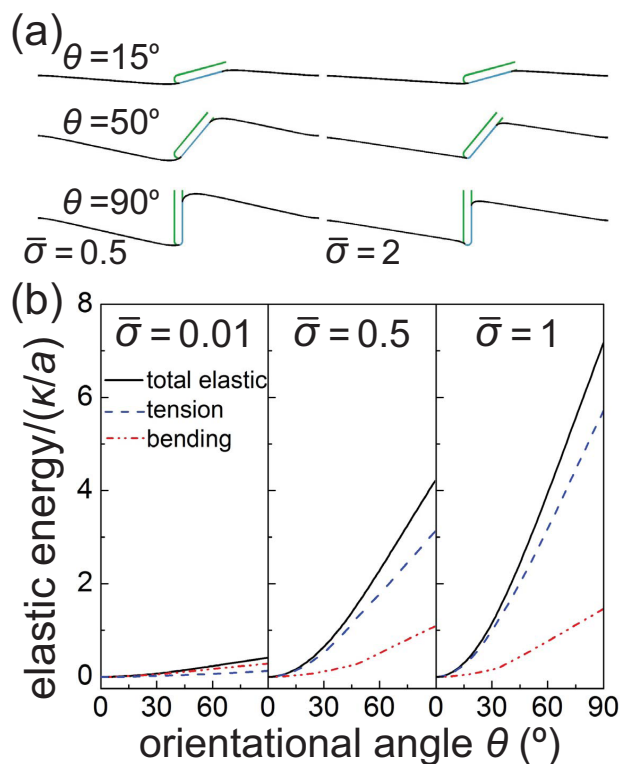


**Fig. 8** (a) Selective configurations of 2D nanomaterials wrapped by cell membranes with  $\bar{\sigma} = 0.5$  and 2 at  $\theta = 30^\circ$ ,  $60^\circ$  and  $90^\circ$ . (b) Variations of rescaled total elastic energy and its two components as a function of  $\theta$  with  $l_c = 3.5\pi a$  for different  $\bar{\sigma}$ . The outer free membrane boundaries are taken as  $\pm 35a$  in (a) and (b).

ric configuration would induce much higher bending energy than the asymmetric configuration. Surface tension tends to flatten the cell membrane to reduce the excess length, which results in the membrane near contact edges having a higher curvature at larger surface tension than at lower surface tension, as demonstrated in Fig. 8a. The rescaled elastic energy  $(E_{\text{tot}} + \gamma l_c)/(\kappa/a)$  is split into two components as rescaled tension energy  $\bar{\sigma}\Delta l/(2a)$  and rescaled bending energy  $E_b/(\kappa/a)$  in eqn (6). Figure 8b shows the total elastic energy and its two components as functions of  $\theta$  at  $\bar{\sigma} = 0.01$ , 0.5 and 1. The membrane tension energy dominates when  $\bar{\sigma} \geq 1$  and the bending energy dominates for an extremely low  $\bar{\sigma}$  ( $\bar{\sigma} \sim 0.01$ ). For intermediate  $\bar{\sigma}$  ( $\bar{\sigma} \sim 0.1$ ), the bending and membrane tension energies make comparable contributions to the total elastic energy. Slight differences are observed between the bending energies at different values of  $\bar{\sigma}$ . In contrast to the energy profiles associated with the penetration mode (see Fig. 4b), the total elastic energy as well as its two components increases with an increasing angle  $\theta$  in the case of the nanomaterial attachment onto membrane, and the configurational torque  $dE_{\text{tot}}/d\theta$  at large  $\theta$  is larger than that at small  $\theta$ . This result, independent of  $\bar{\sigma}$ , points out that adhesive 2D nanomaterials are in favor of parallel adhering with the cell membrane. This is consistent with recent experiments showing that

protein-coated graphene oxide nanosheets attach parallel onto the surface of mouse C2C12 mesenchymal cells,<sup>7</sup> and human THP-1 macrophages adhere to and then spread along a  $25 \mu\text{m}$  few-layer graphene sheet.<sup>1</sup>

Parallel attachment of 2D nanomaterials onto cell membranes is an important cell interaction mode with broad implications for encapsulation, protection, modification, and visualization of cells.<sup>43–45</sup> For example, calcium phosphate layers encapsulating yeast cells can enhance cell viability and protect cells by reducing biological communications with the environment.<sup>43</sup> Calcium-ion functionalized graphene layers as a coating increase stability of yeast cells under exposure to osmotic stresses, and serve as an electrical interface to enable the electron microscopic imaging of cells<sup>45</sup>. Since the conductivity of graphene layers is influenced by their deformation, the graphene coating can also be used to monitor the dynamics of cell surface stresses by measuring the electrical signal through graphene.<sup>45</sup> This is an important biological application as surface stress serves as an indicator of many physiological processes such as cell growth and cell division. Another promising application is designing and building origami-based micropipettes through the assembling and folding of 2D nanomaterials to capture and move target cells.

#### 4 Further discussion on biological implications

Size and surface properties of 2D nanomaterials are essential for their orientation and interaction with cell membranes. MD simulations show that 2D hydrophobic nanomaterials undergo spontaneous membrane piercing at edge asperities or corner sites near-perpendicularly to the cell membrane.<sup>12,13</sup> Our analysis supports that a near-perpendicular configuration with respect to a cell membrane would be adopted by a 2D hydrophobic microsheet when piercing into the cell. The driving force for this near-perpendicular transmembrane configuration mainly originates from splay and membrane tension energies. As the lateral size of the 2D nanomaterial decreases and becomes comparable to the cell membrane thickness, the near-perpendicular configuration could be replaced by a more stable configuration with the whole structure of the 2D nanomaterial positioned parallel along the midplane of the lipid bilayer, resulting in a lower free energy due to the larger attractive interaction area, as reported in MD simulations on the interaction between small pristine or lightly functionalized graphene flakes and lipid bilayers.<sup>12,13,15</sup> The reorientation of 2D nanomaterials between the near-perpendicular transmembrane and parallel embedded configurations would experience an energy barrier due to the deformation and motion of lipid molecules, which is proportional to the size of the 2D nanomaterial. For micro-sized 2D nanomaterials, the energy barrier is too large to be overcome by thermal fluctuation. Therefore, micro-sized 2D nanomaterials, after spontaneous perpendicular piercing at edge asperities or corner sites, would adopt a near-perpendicular transmembrane configuration instead of parallel embedding in the lipid bilayer as small nanoflakes do.

It is noted that the presence of transmembrane 2D nanomaterials might induce the rearrangement of actin networks underneath the cell membrane (especially for macrophages). Although it has been observed that transmembrane graphene microsheets display a near-perpendicular configuration with respect to the surface of murine macrophages,<sup>12</sup> the interaction between 2D nanomaterials and active actin networks is out of the scope of the current study and deserves further investigations.

Depending on the surface properties, 2D nanomaterials can exhibit several different configurations. For example, molecular simulations show that graphene nanoflakes with 5% of edge carbon atoms oxidized to be hydrophilic align parallel in the midplane of the lipid bilayer; while those with 10% edge atoms oxidized adopt a perpendicular transmembrane configuration.<sup>13</sup> The presence of different orientations suggests that parallel embedding and perpendicular transmembrane configurations can serve as possible minimum energy states. In the case of 5% edge atoms oxidized, the attractive interaction due to the larger contact area in the parallel embedding configuration prevails over the repulsion caused by the lightly hydrophilic edges. Therefore, the parallel embedding configuration is the global minimum energy state, similar to the case of pristine graphene flakes. As the edges become highly oxidized (e.g., 10% edge atoms oxidized), the repulsion between the hydrophilic edge atoms and hydrophobic lipid tails dominates over the attractive interaction due to the larger contact area achieved in the parallel configuration, and a near-perpendicular transmembrane configuration becomes energetically favorable. This can be compared to the case of micro-sized 2D nanomaterials, in which the large lateral dimension hinders the appearance of parallel embedding configuration. For hydrophilic 2D nanomaterials or those functionalized with specific molecules binding to the membrane, a parallel adhesive attachment onto the membrane prevails. Similar configurations have been observed in MD simulations of interaction between carbon nanotubes and lipid bilayers.<sup>46</sup>

Regardless of the value of membrane tension, 2D nanomaterials wrapped by a membrane adopt a preferential parallel attachment driven by both bending and membrane tension energies, as our analysis indicates. Two other related but different phenomena are noted here. One is the tension-dependent orientation of a one-dimensional (1D) nanomaterial<sup>39,41</sup> during membrane wrapping and the other is the reorientation and tubulation of nanoparticle aggregates<sup>47</sup> as well as rod-shaped nanoparticles<sup>38,48</sup> wrapped by a membrane. In the case of membrane wrapping of 1D nanomaterials, the bending energy tends to rotate the 1D nanomaterials to a perpendicular configuration ( $\theta = 90^\circ$ ) while the membrane tension energy prefers a parallel configuration ( $\theta \rightarrow 0^\circ$ ).<sup>39</sup> At large  $\bar{\sigma}$ , the tension energy dominates over bending energy and the wrapped 1D nanomaterial exhibits a near-parallel configuration; while at small  $\bar{\sigma}$ , the bending energy dominates and the 1D nanomaterial exhibits a near-perpendicular configuration.<sup>39</sup> In the case of membrane interaction with aggregated<sup>47</sup> or rod-shaped

nanoparticles<sup>38,48</sup>, these nanostructures realign their long axes from a parallel configuration in the early wrapping stage to a perpendicular configuration during the late stage of wrapping. Such an orientational change, which is mainly due to the high membrane bending energy cost at the highly curved regions of the nanostructures, is captured by fully three-dimensional<sup>47,48</sup> as well as two-dimensional<sup>38</sup> studies.

## 5 Conclusions and final remarks

In summary, we have performed theoretical analysis to study two modes of interaction between the cell membrane and micro-sized rigid two-dimensional (2D) nanomaterials: the near-perpendicular transmembrane penetration and parallel attachment onto a membrane. Using a numerical optimization method, we have calculated the system energy profiles as a function of the orientational angle of 2D nanomaterials with respect to the interacting membrane. We find that splay (bending) and membrane tension energies serve as the main driving force for the near-perpendicular (parallel) configuration of transmembrane (membrane attaching) 2D nanomaterials. In contrast, the orientation of one-dimensional nanomaterials wrapped by a cell membrane is tension-dependent, the nanomaterials displaying a perpendicular (parallel) configuration at a small (large) tension.<sup>39</sup> Rotation toward the near-perpendicular configuration makes transmembrane 2D nanomaterials potential candidates for determining lipid membrane viscosity through the measurement of rotation dynamics. Membrane attaching 2D nanomaterials have broad implications including encapsulation, monitoring and manipulation of cells. Elastic 2D nanomaterials as well as those patterned with functional molecules might cause severe local deformation and fusion of cell membranes. Future studies taking into account these effects would be extremely interesting and challenging. Another interesting case related to the present study is the orientation of inserted molecules in a lipid bilayer<sup>49</sup> and one-dimensional transmembrane nanotubes. Molecular dynamics simulations on the membrane translocation of ellipsoidal nanoparticles<sup>50</sup> and nanotube<sup>51,52</sup> and nanoscroll<sup>53</sup> membrane channels have implied a near-perpendicular transmembrane configuration in those cases. However, a comprehensive and dedicated theoretical study on the underlying mechanism remains to be undertaken. The present optimization method based on B-spline parameterization can be generalized to the study of membrane interaction with embedded nanoparticles<sup>54,55</sup> and multiple transmembrane nanomaterials such as proteins.<sup>56,57</sup>

## Acknowledgements

Support from the National Science Foundation under IN-SPIRE: "Computational Design for the Safe Development of High-Aspect-Ratio Nanomaterials", CBET-1344097, and one of its predecessor grants, CMMI-1028530, is gratefully acknowledged.

## References

- 1 V. C. Sanchez, A. Jachak, R. H. Hurt and A. B. Kane, *Chem. Res. Toxicol.*, 2012, **25**, 15–34.
- 2 A. Bianco, *Angew. Chem. Int. Ed.*, 2013, **52**, 4986–4997.
- 3 R. Zhou and H. Gao, *WIREs Nanomed. Nanobi.*, 2014, **6**, 452–474.
- 4 Y. Tu, M. Lv, P. Xiu, T. Huynh, M. Zhang, M. Castelli, Z. Liu, Q. Huang, C. Fan, H. Fang and R. Zhou, *Nat. Nanotechnol.*, 2013, **8**, 594–601.
- 5 K. Yang, J. Wan, S. Zhang, B. Tian, Y. Zhang and Z. Liu, *Biomaterials*, 2012, **33**, 2206–2214.
- 6 Y. Chang, S.-T. Yang, J.-H. Liu, E. Dong, Y. Wang, A. Cao, Y. Liu and H. Wang, *Toxicol. Lett.*, 2011, **200**, 201–210.
- 7 Q. Mu, G. Su, L. Li, B. O. Gilbertson, L. H. Yu, Q. Zhang, Y.-P. Sun and B. Yan, *ACS Appl. Mater. Interfaces*, 2012, **4**, 2259–2266.
- 8 Y. Li, Y. Liu, Y. Fu, T. Wei, L. Le Guyader, G. Gao, R.-S. Liu, Y.-Z. Chang and C. Chen, *Biomaterials*, 2012, **33**, 402–411.
- 9 G.-Y. Chen, H.-J. Yang, C.-H. Lu, Y.-C. Chao, S.-M. Hwang, C.-L. Chen, K.-W. Lo, L.-Y. Sung, W.-Y. Luo, H.-Y. Tuan and Y.-C. Hu, *Biomaterials*, 2012, **33**, 6559–6569.
- 10 K.-H. Liao, Y.-S. Lin, C. W. Macosko and C. L. Haynes, *ACS Appl. Mater. Interfaces*, 2011, **3**, 2607–2615.
- 11 R. Frost, G. E. Jonsson, D. Chakarov, S. Svedhem and B. Kasemo, *Nano Lett.*, 2012, **12**, 3356–3362.
- 12 Y. Li, H. Yuan, A. von dem Bussche, M. Creighton, R. H. Hurt, A. B. Kane and H. Gao, *Proc. Natl. Acad. Sci. U.S.A.*, 2013, **110**, 12295–12300.
- 13 J. Wang, Y. Wei, X. Shi and H. Gao, *RSC Advances*, 2013, **3**, 15776–15782.
- 14 A. V. Titov, P. Král and R. Pearson, *ACS Nano*, 2010, **4**, 229–234.
- 15 R. Guo, J. Mao and L.-T. Yan, *Biomaterials*, 2013, **34**, 4296–4301.
- 16 W. Helfrich, *Z. Naturforsch. C*, 1973, **28**, 693–703.
- 17 A. Ben-Shaul, In *Structure and Dynamics of Membranes*, ed. R. Lipowsky and E. Sackmann, Elsevier, Amsterdam, 1995, ch. 7, pp. 359–401.
- 18 M. Hamm and M. M. Kozlov, *Eur. Phys. J. B*, 1998, **6**, 519–528.
- 19 M. Hamm and M. M. Kozlov, *Eur. Phys. J. E*, 2000, **3**, 323–335.
- 20 Y. Kozlovsky and M. M. Kozlov, *Biophys. J.*, 2002, **82**, 882–895.
- 21 S. May, *Biophys. J.*, 2002, **83**, 2969–2980.
- 22 S. May and A. Ben-Shaul, *Biophys. J.*, 1999, **76**, 751–767.
- 23 M. Ø. Jensen and O. G. Mouritsen, *Biochim. Biophys. Acta*, 2004, **1666**, 205–226.
- 24 D. Marsh, *Biophys. J.*, 2008, **94**, 3996–4013.
- 25 Z. Chen and R. P. Rand, *Biophys. J.*, 1997, **73**, 267–276.
- 26 R. E. Tosh and P. J. Collings, *Biochim. Biophys. Acta*, 1986, **859**, 10–14.
- 27 S. May, *Eur. Biophys. J.*, 2000, **29**, 17–28.
- 28 W. Rawicz, K. C. Olbrich, T. McIntosh, D. Needham and E. Evans, *Biophys. J.*, 2000, **79**, 328–339.
- 29 P. Wiggins and R. Phillips, *Proc. Natl. Acad. Sci. U.S.A.*, 2004, **101**, 4071–4076.
- 30 G. Farin, *Curves and Surfaces for CAGD: A Practical Guide*, Morgan Kaufmann, San Francisco, 5th edn., 2002.
- 31 J. Nocedal and S. J. Wright, *Numerical Optimization*, Springer, New York, 2nd edn., 2006.
- 32 C. Nielsen, M. Goulian and O. S. Andersen, *Biophys. J.*, 1998, **74**, 1966–1983.
- 33 C. Nielsen and O. S. Andersen, *Biophys. J.*, 2000, **79**, 2583–2604.
- 34 J. M. Yuk, J. Park, P. Ercius, K. Kim, D. J. Hellebusch, M. F. Crommie, J. Y. Lee, A. Zettl and A. P. Alivisatos, *Science*, 2012, **6**, 61–64.
- 35 J. Shi, J. Chen and P. S. Cremer, *J. Am. Chem. Soc.*, 2008, **130**, 2718–2719.
- 36 T. R. Weikl, *Eur. Phys. J. E*, 2003, **12**, 265–273.
- 37 X. Yi, X. Shi and H. Gao, *Phys. Rev. Lett.*, 2011, **107**, 098101.
- 38 X. Yi and H. Gao, *Phys. Rev. E*, 2014, **89**, 062712.
- 39 X. Yi, X. Shi and H. Gao, *Nano Lett.*, 2014, **14**, 1049–1055.
- 40 H. Gao, W. Shi and L. B. Freund, *Proc. Natl. Acad. Sci. U.S.A.*, 2005, **102**, 9469–9474.
- 41 X. Shi, A. von dem Bussche, R. H. Hurt, A. B. Kane and H. Gao, *Nat. Nanotech.*, 2011, **6**, 714–719.
- 42 W. T. Gózdź, *J. Phys. Chem. B*, 2005, **109**, 21145–21149.
- 43 B. Wang, P. Liu, W. Jiang, H. Pan, X. Xu and R. Tang, *Angew. Chem. Int. Ed.*, 2008, **47**, 3560–3564.
- 44 N. Mohanty, M. Fahrenholtz, A. Nagaraja, D. Boyle and V. Berry, *Nano Lett.*, 2011, **11**, 1270–1275.
- 45 R. Kempaiah, A. Chung and V. Maheshwari, *ACS Nano*, 2011, **5**, 6025–6031.
- 46 S. Baoukina, L. Monticelli and D. P. Tieleman, *J. Phys. Chem. B*, 2013, **117**, 12113–12123.
- 47 A. H. Bahrami, R. Lipowsky and T. R. Weikl, *Phys. Rev. Lett.*, 2012, **109**, 188102.
- 48 A. H. Bahrami, *Soft Matter*, 2013, **9**, 8642–8646.
- 49 A. Kessel, N. Ben-Tal and S. May, *Biophys. J.*, 2001, **81**, 643–658.
- 50 K. Yang and Y.-Q. Ma, *Nat. Nanotechnol.*, 2010, **5**, 579–583.
- 51 S. O. Nielsen, B. Ensing, V. Ortiz, P. B. Moore and M. L. Klein, *Biophys. J.*, 2005, **88**, 3822–3828.
- 52 B. Liu, X. Li, B. Li, B. Xu and Y. Zhao, *Nano Lett.*, 2009, **9**, 1386–1394.
- 53 X. Shi, Y. Cheng, N. M. Pugno and H. Gao, *Small*, 2010, **6**, 739–744.
- 54 G. K. Xu, X. Q. Feng and S. W. Yu, *Nano Res.*, 2010, **3**, 356–362.
- 55 Y. Li, X. Li, Z. Li and H. Gao, *Nanoscale*, 2012, **4**, 3768–3775.
- 56 T. R. Weikl, M. M. Kozlov and W. Helfrich, *Phys. Rev. E*, 1998, **57**, 6988–6995.
- 57 K. Bohinc, V. Kralj-Iglič and S. May, *J. Chem. Phys.*, 2003, **119**, 7435–7444.